



HAL
open science

Imaging the crustal and upper mantle structure of the North Anatolian Fault: A Transmission Matrix Framework for Local Adaptive Focusing

Rita Touma, Arthur Le Ber, Michel Campillo, Alexandre Aubry

► To cite this version:

Rita Touma, Arthur Le Ber, Michel Campillo, Alexandre Aubry. Imaging the crustal and upper mantle structure of the North Anatolian Fault: A Transmission Matrix Framework for Local Adaptive Focusing. 2023. hal-04027628v1

HAL Id: hal-04027628

<https://hal.science/hal-04027628v1>

Preprint submitted on 13 Mar 2023 (v1), last revised 17 Oct 2023 (v2)

HAL is a multi-disciplinary open access archive for the deposit and dissemination of scientific research documents, whether they are published or not. The documents may come from teaching and research institutions in France or abroad, or from public or private research centers.

L'archive ouverte pluridisciplinaire **HAL**, est destinée au dépôt et à la diffusion de documents scientifiques de niveau recherche, publiés ou non, émanant des établissements d'enseignement et de recherche français ou étrangers, des laboratoires publics ou privés.



Distributed under a Creative Commons CC0 - Public Domain Dedication 4.0 International License

Imaging the crustal and upper mantle structure of the North Anatolian Fault: A Transmission Matrix Framework for Local Adaptive Focusing

Rita Touma,^{1,2} Arthur Le Ber,¹ Michel Campillo,² and Alexandre Aubry¹

¹*Institut Langevin, ESPCI Paris, PSL University, CNRS, Paris, France*

²*ISTerre, Université Grenoble Alpes, Maison des Géosciences, BP 53, F-38041 Grenoble, France*

(Dated: March 10, 2023)

Abstract

Imaging the structure of major fault zones is essential for our understanding of crustal deformations and their implications on seismic hazards. Investigating such complex regions presents several issues, including the variation of seismic velocity due to the diversity of geological units and the cumulative damage caused by earthquakes. Conventional migration techniques are in general strongly sensitive to the available velocity model. Here we apply a passive matrix imaging approach which is robust to the mismatch between this model and the real seismic velocity distribution. This method relies on the cross-correlation of ambient noise recorded by a geophone array. The resulting set of impulse responses form a reflection matrix that contains all the information about the subsurface. In particular, the reflected body waves can be leveraged to: (i) determine the transmission matrix between the Earth's surface and any point in the underground; (ii) build a confocal image of the underground reflectivity with a transverse resolution only limited by diffraction. As a study case, we consider seismic noise (0.1-0.5 Hz) recorded by the Dense Array for Northern Anatolia (DANA) that consists of 73 stations deployed for 18 months in the region of the 1999 Izmit earthquake. Passive matrix imaging reveals the scattering structure of the crust and upper mantle around the NAFZ over a depth range of 60 km. The results show that most of the scattering is associated with the Northern branch that passes throughout the crust and penetrates into the upper mantle.

I. Introduction

The North Anatolian Fault zone (NAFZ) is one of the major continental right-lateral strike slip faults, and forms a border between the Eurasian continent and the Anatolian block. With an extremely well developed surface expression, it is one of the most active faults in the Eastern Mediterranean region [1, 2]. It is over 1600 km long and extends from eastern Turkey in the east to Greece in the west and historically has been subject to many destructive earthquakes [3, 4]. The seismic activity of such large faults constitutes a continuous hazard/threat to the surrounding regions and big cities, especially Istanbul city located to the West of the fault.

Faults are well defined at the surface by the localized deformation and displacement delineating the fault traces, but its deep structure remains poorly understood [5]. The understanding of such major fault systems and seismic hazard requires a characterization of the geometrical and seismic properties of the crust and upper mantle. A large number of geological and geophysical studies discussed the complexity of fault zones and their relation with their deep roots [4]. They are not

only confined in the mid crust, indeed, models suggest that they penetrate deep into the crust and extend to the upper Mantle. If so, faults develop into shear zones, corresponding to a volume of localized deformation accounting for the relative displacement of the tectonic blocks.

Seismic imaging techniques, especially reflection, refraction, and tomographic methods, constitute a very powerful tool to characterize fault zones and report the variation of the properties of the crust and the upper mantle. They rely on the study of wave propagation inside the Earth that is governed by the density and elastic properties of the rocks. To properly probe the medium, waves should be generated by a dense distribution of seismic sources. Conventional seismic exploration techniques use either the earthquakes as seismic source, or explosions and vibrators to generate seismic waves in regions with weak seismicity. Because of the limitations in the earthquake distribution and high cost of active methods, there was a need for alternative imaging approaches that would not rely on any coherent source. In the 2000's, the extraction of deterministic information about the Earth structure from ambient seismic noise revolutionized the field of seismology [see e.g. 6]. It was shown that the cross-correlation of diffuse waves or ambient seismic noise recorded at two stations provides the Green's function between those two stations [see e.g. 7]. The reflection response of the medium is then retrieved and can be applied to build tomographic or structural images of the Earth. Because ambient noise is dominated by surface waves, their Green's function component can be easily extracted [8]. It has been proved that body wave reflections can also be retrieved from ambient seismic noise cross-correlations [9–11]. Body waves contain valuable information on the structure of the medium in depth and can be investigated to obtain high-resolution images of the crust and the mantle [12].

Faults are usually imaged indirectly through strong velocity contrasts in tomographic profiles [13], or through the offset of geological layers observed in reflectivity images [14]. However, tomographic images exhibit a relatively bad resolution, while reflection imaging methods are strongly sensitive to the available velocity model. Interestingly, a reflection matrix approach has been recently proposed to cope with these issues. Originally developed in acoustics [15, 16] and optics [17, 18], this approach has been recently applied to passive seismology [19, 20]. By considering high frequency seismic noise (10-20 Hz), high resolution images of complex areas, such as volcanoes [21] and fault zones [20], have been obtained over a few km depth. In this paper, we aim to characterize the crustal structure of the NAFZ at a much larger scale (until 60 km depth). To that aim, a lower frequency bandwidth (0.1-0.5 Hz) has been considered. At the corresponding wavelengths, the subsurface reflectivity can be considered as continuous rather than

being seen as a discrete distribution of scatterers as in our previous works [20, 21]. As we will see, this continuous but random reflectivity can be exploited to enable a local and adapted auto-focus on each part of the subsurface image, thereby showing an important robustness to the inaccuracy of the initial wave velocity model.

Seismic matrix imaging is based on the passive measurement of the reflection matrix \mathbf{K} associated with a network of geophones. It contains the set of impulse responses between each geophone extracted from cross-correlations of seismic noise. Based on the available velocity model, a focused reflection (FR) matrix is built by applying a redatuming process to \mathbf{K} [15, 19]. It contains the impulse response between virtual sources and receivers synthesized inside the medium. This FR matrix is powerful as it provides: (i) a confocal image of the subsurface along its diagonal; (ii) a local quantification of aberrations in the vicinity of each virtual source from its off-diagonal elements. In contrast with previous works [20, 21], a multi-layered wave velocity model is here considered rather than just an homogeneous model. This more sophisticated description of seismic wave propagation enables a better time-to-depth conversion in the confocal image and a better focusing process. Nevertheless, the FR matrix still highlights residual aberrations that result from the mismatch between the velocity model and the actual velocity distribution. The fluctuations of wave velocities actually induce phase distortions on the focused wave-fronts that result in a blurry image of the NAFZ underground.

To overcome these detrimental effects, the FR matrix can be first projected in a plane wave basis. By exploiting the angular input-output correlations of the reflection matrix, phase distortions of the incident and reflected wave-front can be identified and compensated. This is the principle of the CLASS algorithm (acronym for closed-loop accumulation of single scattering), originally developed in optical microscopy [17, 22, 23]. Applied for the first time to seismology in the present study, CLASS successfully compensates for spatially-invariant aberrations and will be shown to clearly improve the confocal image of the NAFZ subsurface.

Nevertheless, high-order aberrations subsist and are addressed through the distortion matrix concept in a second step. Originally introduced in ultrasound imaging [16] and optical microscopy [18], this operator contains the phase distortions of the incident and reflected wave-fronts with respect to the propagation model. It was recently exploited in passive seismology in order to image the San Jacinto Fault zone scattering structure that exhibits a sparse distribution of scatterers [20]. Here, we apply it in a new scattering regime since the NAFZ subsurface exhibits, in the frequency range under study, a continuous reflectivity distribution made of specular reflectors

and randomly distributed heterogeneities. In this regime, a local time reversal analysis of the distortion matrix can be performed in order to retrieve the transmission matrix between the Earth's surface and any point of the subsurface [24]. This transmission matrix is a key tool since its phase conjugate provides the optimized focusing laws that need to be applied to the reflection matrix in order to retrieve a diffraction-limited image of the subsurface. While most conventional reflection imaging techniques are strongly sensitive to the available velocity model, the reflection matrix approach is robust with respect to the inaccuracy of this model. An approximate velocity distribution is actually sufficient since a time-reversal analysis of seismic data enables a local and adapted auto-focus on each part of the subsurface image.

To image the crustal structure of NAFZ, we use data from the Dense Array for Northern Anatolia that was deployed over the western segment of the fault, in the latest rupture region during the 1999 Izmit ($M = 7.6$) and Düzce ($M = 7.2$) earthquakes [25, 26]. The dense array was installed temporarily between May 2012 and October 2013. It consists of 73 3-component broadband seismometers, 66 stations arranged along 11 east-west lines and 6 North-South lines forming a rectangular grid and covering an area of 35 km by 70 km with a nominal inter-stations spacing of ~ 7 km (Fig. 1a). Seven additional stations were deployed east of the rectangular array in a semi-circle shape. In this region, the fault splits into two major strands: the northern (NNAFZ) and southern (SNAFZ) strands (Fig. 1b). The northern strand, where most of the continuous deformation occurs according to geodetic studies [2, 27], has been subject to a series of major earthquakes in the last century, among them the 1999 Izmit Earthquake. On the contrary, the latest rupture of the southern branch dates back to the fifteenth century [28]. The fault delineates three tectonic blocks (Fig. 1b): (i) the Istanbul Zone (IZ) situated North of the northern branch, (ii) the Sakarya zone (SZ) situated to the South of the southern branch and (iii) the Armutlu-Almacik crustal block (AA) located in the center, between the two fault strands [29–31]. Differences in crustal composition and properties between these blocks have been reported. Strong velocity contrasts were found across the fault strands by several tomographic studies [32–35] and full waveform inversion studies [36, 37]. Low velocity zones are found below the surface traces of the SNAFZ and NNAFZ [34, 35]. The crust of Istanbul and Armutlu Blocks is characterized by high velocities while SZ shows relatively low velocities [33–35, 38].

The present study reveals the 3D scattering structure of the medium below this major fault. It does not only image planar interfaces, but provides a direct insight on the heterogeneities that mainly sit in the vicinity of the strands. The observed results complement previous studies con-

ducted in the region. A step in the Moho is detected below the Northern branch, and several sub-Moho structures are observed in the North confirming that the northern branch penetrates in the upper mantle. The southern strand does not have a strong signature in the scattering profiles.

II. Passive Seismic Matrix Imaging

A. Reflection matrix in the geophones basis

To apply matrix imaging, we used the ambient seismic noise recorded at DANA (see Fig. 1) to compute the cross-correlation functions of horizontal EE component over the 18 months of recording period. Considering the body wave component, this implies that the waves being dealt with are shear waves that have been reflected. First, the data were down-sampled at 25 Hz and corrected from instrument response. Then, the data were split into one-hour windows. Each window is band-pass filtered between 0.1 and 0.5 Hz after applying a spectral whitening between 0.01 and 1 Hz [39]. The cross-correlation between every pair of stations is computed over the one-hour windows and finally stacked to obtain the mean cross-correlation function. Although, considering noise in a higher frequency range would allow, in principle, to improve the resolution of the images, matrix imaging requires the Nyquist criterion to be fulfilled: The inter-station distance (7 km) shall be of the order of a half-wavelength. Considering a S-wave velocity $c_0 = 1700$ m/s near the surface, this criterion led us to choose the 0.1 – 0.5 Hz frequency range ($\lambda = 5.7$ km at the central frequency). The ambient noise energy in the frequency band considered in this study comes from the secondary microseisms (5 – 10 s period band) originated by the ocean [40–42] and constitutes one of the most energetic parts of the seismic noise.

The symmetric cross-correlations can be stacked in a time-dependent response matrix $\mathbf{K}(t)$. One element $k_{ij}(t)$ of this matrix corresponds to the impulse response between geophones i and j . In other words, $k_{ij}(t)$ contains the seismic wave-field recorded at receiver i if a pulse was emitted by the virtual source j at time $t = 0$. This response includes not only direct arrivals, but also all the seismic wave-field scattered by the medium. The latter component can be used to retrieve local information on the medium’s reflectivity. The scattered wave-field itself can be decomposed into two components: (i) a single-scattering contribution that is useful for imaging the scattering structure of the medium, and (ii) a multiple scattering contribution that is very detrimental for imaging purposes and results in spurious arrivals and ghosts in the reflectivity images. Fortunately,

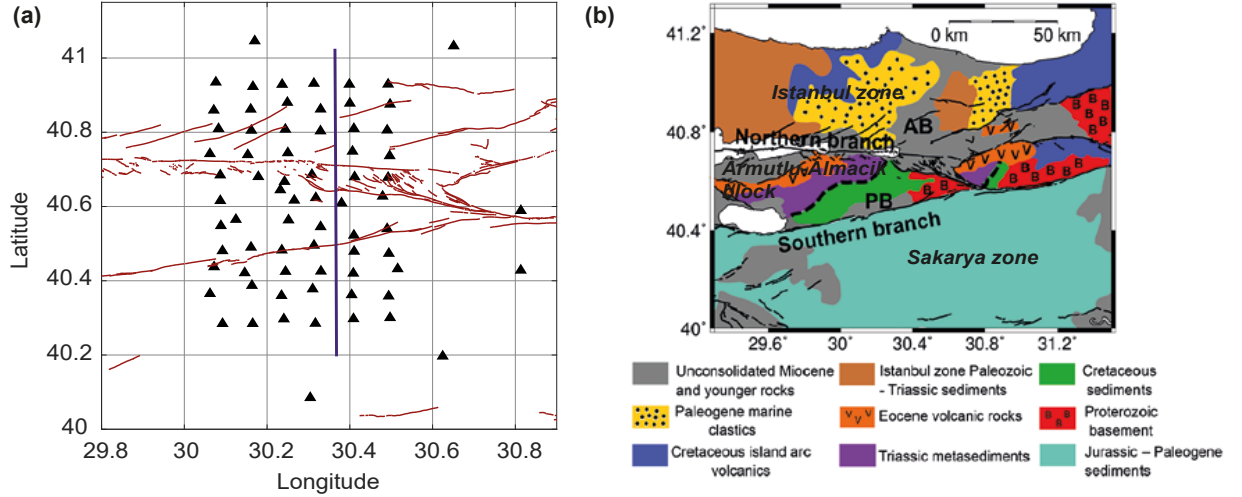


FIG. 1: Study region and location of DANA array. (a) Map of the study region and location of DANA array geophones (black triangle). The surface traces of the NAFZ are represented by the red lines [43]. The blue line indicate the location of the cross sections represented in Figs. 3a1 and a2. (b) Geological map of the region (adjusted from [38] and [44]). The major geological blocks are represented: Istanbul zone (IZ) in the North, Armutlu-Almacik (AA) block in the center and Sakarya zone (SZ) in the South. The Adapazari and Pamukova basin location are indicated by AB and PB, respectively.

the latter contribution is here negligible compared to the single scattering component, as we will see in the next section.

B. Redatuming process

An image of the medium reflectivity can be obtained by applying a double focusing operation to $\mathbf{K}(t)$ [19, 20]. It consists in back-propagating the response measured at the surface into wave-fields below the surface as if there were sources and receivers inside the medium. This is similar to the "wave-field extrapolation" concept that forms the basis of the migration process [45]. It requires performing beamforming operations both at emission and reception. On the one hand, focusing in emission consists in applying appropriate time delays to the emitted sources so that waves constructively interfere and focus on one point inside the medium. Physically, this operation amounts to synthesize a virtual source inside the medium. On the other hand, focusing in reception is carried out by applying proper time delays to the received signals so that they can constructively interfere. As in emission, this focusing operation can be seen as the synthesis of a virtual receiver inside the medium. This operation is known as "redatuming" in seismology [46] and consists of

virtually moving sources and receivers from the surface to the medium below (Fig. 2a). Generally, an image of the sub-surface is built by considering the response of virtual source and receiver placed at the same location (Fig. 2f). On the contrary, the principle of matrix imaging consists in decoupling both locations [15].

In the following, the reflection matrix will be expressed in three different bases: *(i)* the geophones basis where the matrix \mathbf{K} represents the cross-correlations between all pairs of stations located at $\mathbf{s}(x_s, y_s, 0)$, *(ii)* the focused basis corresponding to the location $\mathbf{r}(x, y, z)$ of virtual sources and receivers synthesized by the focusing operations and in which the image of the medium is built, and *(iii)* the spatial Fourier basis $\mathbf{k}_{||}(k_x, k_y)$ that will be first used for wave-field extrapolation and then for aberration correction.

C. Propagator from the geophones to the focused basis

The focusing operations described in section II B shall provide the FR matrix that plays a pivotal role in matrix imaging. We now show how this matrix can be obtained through simple matrix operations.

Mathematically, the response between virtual sources and receivers is obtained from the response matrix at the surface through the Green's functions, that describe the propagation between each geophone and each point inside the medium using a wave velocity model. Switching between bases can be easily achieved by simple matrix products in the frequency domain. Consequently, a temporal Fourier transform is first applied to the measured response matrix $\mathbf{K}(t)$. For each frequency in the bandwidth of interest, a monochromatic matrix $\mathbf{K}(f)$ is obtained. We then define the propagator $\mathbf{T}_0(z, f)$, that enables a direct projection of the response matrix from the geophones' basis to the focused basis $\boldsymbol{\rho} = (x, y)$ at each depth z . Each monochromatic response matrix $\mathbf{K}(f)$ can be projected in the focused basis both at input and output by applying appropriate phase shifts associated with downgoing waves at input and upgoing waves at output to provide the FR matrix $\mathbf{R}_{\boldsymbol{\rho}\boldsymbol{\rho}}$ (Fig. 2a). Under a matrix formalism, this matrix can be obtained by the following matrix product:

$$\mathbf{R}_{\boldsymbol{\rho}\boldsymbol{\rho}}(z, f) = \mathbf{T}_0^\dagger(z, f) \times \mathbf{K}(f) \times \mathbf{T}_0^*(z, f). \quad (1)$$

A model for the wave velocity distribution inside the medium is required. In this study, and since the horizontal EE cross-correlation functions are considered, only an estimation of the S-

wave velocity is required. Unlike [19] and [20] that considered a homogeneous P-wave velocity model, here a layered 1-D S-wave velocity model is used for the focusing process. A combination of two models derived by [47], for the first 5 km, and by [48], for deeper layers is displayed in Table I. Compared to an homogeneous model, such a layered model will allow a better time-depth conversion and will limit the aberration level in the subsurface image.

Layer # i	Depth (km)	c_i (m s ⁻¹)
0	0 - 1	1700
1	1 - 3.5	2500
2	3.5 - 14	3200
3	14 - 26	3500
4	26 - 40	3600
5	40 - 60	4300

TABLE I: 1-D S-wave velocity model. c_i versus depth following [48] and [47].

In a layered medium, the forward and backward extrapolation of the reflection matrix is performed through the decomposition of the wave-field into plane waves [45]. Indeed, plane waves can be easily extrapolated by applying a simple phase shift. The decomposition of the wave-field recorded at $z = 0$ into plane waves can be done by considering the spatial Fourier transform operator $\mathbf{P}_0 = [P_0(\mathbf{s}, \mathbf{k}_{||})]$ that connects the geophone's position \mathbf{s} to the transverse component $\mathbf{k}_{||} = (k_x, k_y)$ of the wave vector:

$$P_0(\mathbf{s}, \mathbf{k}_{||}) = \exp(i\mathbf{k}_{||} \cdot \mathbf{s}), \quad (2)$$

The symbol \cdot denotes a scalar product. We then define the spatial transfer function $\exp(-ik_z^{(i)}\Delta z_i)$, that models the ballistic propagation of the seismic wave through the i^{th} layer with

$$k_z^{(i)} = \sqrt{\left(\frac{2\pi f}{c_i}\right)^2 - k_x^2 - k_y^2},$$

the longitudinal component of the wave vector \mathbf{k} in the i^{th} layer, c_i the wave velocity in the i^{th} layer of our model and Δz_i its thickness. To propagate the plane waves from the surface to depth z , we define the wave-field extrapolator, $\mathbf{F}(z, f) = [F(\mathbf{k}, z, f)]$, as the product of the spatial transfer function of the N layers above the considered depth as follows:

$$F(\mathbf{k}_{\parallel}, z, f) = \exp(-ik_z^{(N)}(z - z_N)) * \prod_{i=1}^{N-1} \exp(-ik_z^{(i)}\Delta z_i), \quad (3)$$

where z_i is the depth at which starts the i^{th} layer. The far field propagator, $\mathbf{T}(z, f) = [T(\mathbf{s}, \mathbf{r}, z, f)]$, can finally be expressed as follows:

$$\mathbf{T}_0(z, f) = [\mathbf{P}_0 \circ \mathbf{F}(z, f)] \times \mathbf{P}'_0{}^\dagger. \quad (4)$$

where the symbols \dagger and \circ stands for transpose conjugate and Hadamard product, respectively. $\mathbf{P}'_0 = [P'_0(\boldsymbol{\rho}, \mathbf{k}_{\parallel})]$ corresponds to the Fourier transform operator linking the focused and plane wave bases. It connects the transverse wave vector $\mathbf{k}_{\parallel} = (k_x, k_y)$ of each plane wave to the transverse coordinates $\boldsymbol{\rho} = (x, y)$ of each focusing point:

$$\mathbf{P}'_0(\boldsymbol{\rho}, \mathbf{k}_{\parallel}) = \exp(i\mathbf{k}_{\parallel} \cdot \boldsymbol{\rho}). \quad (5)$$

To avoid aliasing during the change of basis between the plane wave and focused bases, a Shannon criterion should be respected. The wave numbers k_x and k_y are supposed to fulfill the following condition:

$$\sqrt{k_x^2 + k_y^2} < k_0, \quad (6)$$

with k_0 the wave number at the Earth surface. The resolution δk of the Fourier plane is conditioned by the size of the array $\mathcal{D} = 50$ km such that $\delta k = 2\pi/\mathcal{D}$. By properties of the Fourier transform, the transverse resolution $\delta\rho_0$ in the focal plane, that corresponds to the distance between the focusing points \mathbf{r} , is chosen to be $\sim \lambda_{\min}/2 \sim 2$ km to circumvent spatial aliasing in the focused basis.

D. Broadband focused reflection matrix

Under the matrix formalism, time gating can be performed by building a broadband FR matrix $\mathbf{R}_{\rho\rho}(z)$. This matrix is obtained by integrating $\mathbf{R}_{\rho\rho}(z, f)$ over the frequency bandwidth:

$$\mathbf{R}_{\rho\rho}(z) = \int_{f_1}^{f_2} df \mathbf{T}_0^\dagger(z, f) \times \mathbf{K}(f) \times \mathbf{T}_0^*(z, f), \quad (7)$$

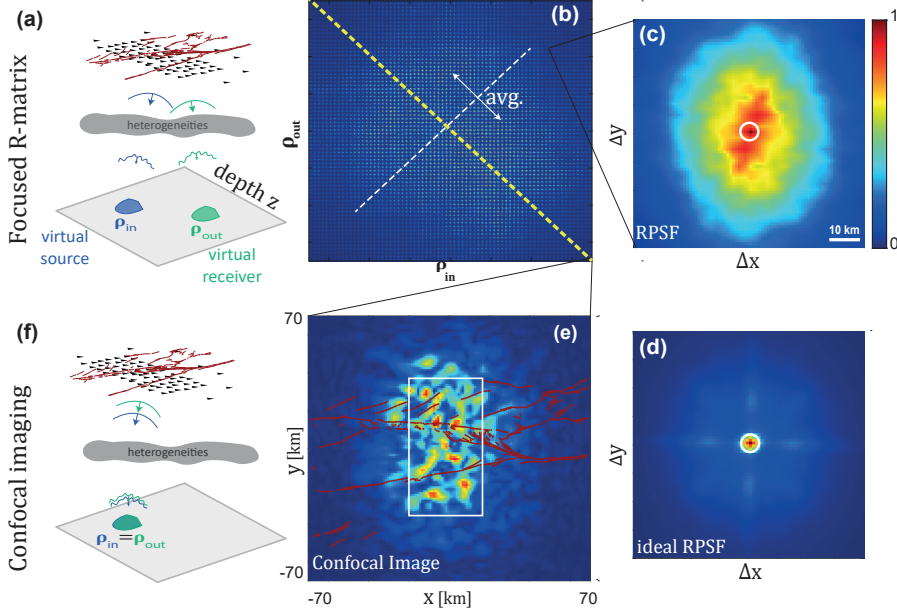


FIG. 2: Focused reflection matrix. (a) The response matrix \mathbf{K} is projected onto a focused basis at each depth z (Eq. 7), thereby synthesizing a set of virtual sources ($\boldsymbol{\rho}_{\text{in}}$) and receivers ($\boldsymbol{\rho}_{\text{out}}$) scanning laterally the field-of-view. In presence of fluctuations in the seismic velocity, focused waves are distorted while travelling from the surface to the plane, thereby enlarging and distorting the virtual geophones. (b) This effect gives rise to a off-diagonal spreading of backscattered energy in the focused reflection matrix $\mathbf{R}_{\rho\rho}(z)$ shown here at depth $z = 25$ km. (c) The corresponding intensity profile, averaged over whole the field-of-view, provides the so-called RPSF I (Eq. 12). The white circle represents the diffraction-limited transverse resolution ($\delta\rho_0 \sim 6$ km) at the considered depth. (d) The ideal RPSF that would be obtained in absence of aberrations is shown for comparison (e) Confocal image \mathcal{I} (Eq. 10) built from the diagonal of $\mathbf{R}_{\rho\rho}$. The white box represents the dimensions of the rectangular array of geophones and the red lines represent the NAFZ fault traces at the surface. (f) The confocal image corresponds to a simultaneous focusing process at input and output ($\mathbf{r}_{\text{in}} = \mathbf{r}_{\text{out}}$). In panels (b)-(e), the color scale refers to the scattering intensity. It is normalized by the maximum value of the scattering energy at the considered depth.

with $f_1 = 0.1$ Hz and $f_2 = 0.5$ Hz. The symbol $*$ stands for phase conjugate. This operation amounts to do an inverse Fourier transform at time $t = 0$ over the frequency band $[0.1 \text{ } 0.5]$ Hz. Physically, it corresponds to a ballistic time gating that tends to select singly-scattered waves associated with a scattering event in the focal plane. Each coefficient $R(\boldsymbol{\rho}_{\text{out}}, \boldsymbol{\rho}_{\text{in}}, z)$ of $\mathbf{R}_{\rho\rho}(z)$ contains the wave-field that would be recorded by a virtual geophone located at $\mathbf{r}_{\text{out}} = (\boldsymbol{\rho}_{\text{out}}, z)$ if a virtual source at $\mathbf{r}_{\text{in}} = (\boldsymbol{\rho}_{\text{in}}, z)$ emits a pulse of length $\delta t = \Delta f^{-1}$ at the central frequency f_0 , with $\Delta f = f_2 - f_1 = 0.4$ Hz.

The FR matrix can be expressed theoretically as follows [15, 20, 49]:

$$\mathbf{R}_{\rho\rho}(z) = \mathbf{H}^\top(z) \times \Gamma(z) \times \mathbf{H}(z), \quad (8)$$

or, in terms of matrix coefficients,

$$R(\boldsymbol{\rho}_{\text{out}}, \boldsymbol{\rho}_{\text{in}}, z) = \int d\mathbf{r} H(\boldsymbol{\rho}, \boldsymbol{\rho}_{\text{out}}, z) \gamma(\boldsymbol{\rho}, z) H(\boldsymbol{\rho}, \boldsymbol{\rho}_{\text{in}}, z). \quad (9)$$

$\mathbf{H}(z) = \mathbf{P}'_0 \times \mathbf{T}(z)$ is the focusing matrix that contains the point spread functions $H(\boldsymbol{\rho}, \boldsymbol{\rho}_{\text{in/out}}, z)$ around each focusing point $\mathbf{r}_{\text{in/out}} = (\boldsymbol{\rho}_{\text{in/out}}, z)$ in the field-of-view and $\mathbf{T}(z) = [T(\mathbf{k}_{\parallel}, \boldsymbol{\rho}, z)]$ is the true transmission matrix that describes wave propagation between the focused and the Fourier bases. The amplitude distribution of $H(\boldsymbol{\rho}, \boldsymbol{\rho}_{\text{in/out}}, z)$ accounts for the lateral extent of each virtual source/detector at $\mathbf{r}_{\text{in/out}}$. Eq 9 confirms that the diagonal elements of $\mathbf{R}_{\rho\rho}$ form an estimator of the subsurface reflectivity: it results from the convolution between the true reflectivity and H^2 , the confocal PSF.

An example of the broadband FR matrix $\mathbf{R}_{\rho\rho}$ is shown at depth $z = 25$ km in Fig. 2b. $\mathbf{R}_{\rho\rho}$ is a four-dimension matrix concatenated in 2D as a set of blocks [19]. As in the SJFZ study [20], the backscattered energy is far from being concentrated along the diagonal of $\mathbf{R}_{\rho\rho}$, which would be ideally the case if the wave velocity model was correct. The spreading of the backscattered energy outside the diagonal is a manifestation of phase distortions due to lateral variations of shear velocity that is not accounted for by the multi-layered wave velocity model in Table I. Nevertheless, one can build an image of the medium reflectivity at effective depth z by considering the diagonal elements of the FR matrix that correspond to identical focusing points at input and output (Fig. 2f). It yields the following *confocal* image:

$$\mathcal{I}(\boldsymbol{\rho}, z) = |R(\boldsymbol{\rho}, \boldsymbol{\rho}, z)|^2. \quad (10)$$

Fig. 2e shows the resulting 2D image \mathcal{I} at $z = 25$ km retrieved from the diagonal of the FR matrix in Fig. 2b. Such an image is an estimator of the reflectivity at depth z with a transverse resolution that would be ideally only limited by diffraction [50]:

$$\delta\rho_0 = \lambda/(2 \sin \theta) \quad (11)$$

where $\theta = \arctan(\mathcal{D}/2z)$ is determined by the size of the array $\mathcal{D} = 50$ km, and corresponds to the maximum angle under which a focusing point sees the geophones' array. By stacking the confocal

image computed at each depth z , a 3D image of the reflectivity can be obtained. The cross-section at Lon 30.37° is displayed in Fig. 3a₁. 2D *confocal* images at $z = 15, 30$ and 40 km are also shown in Fig. 3b₁. Unlike the transverse resolution, the axial resolution δz is limited by the frequency bandwidth: $\delta z \sim c/\Delta f \sim 8.7$ km, with c the shear wave velocity at the considered depth. The sections of the 3D image displayed in Figs. 2e, 3a and 3b show a greater reflectivity in the central part of the field-of-view, i.e right below the geophones' array, but no direct correlation can be found between the image and the location of the fault strands. In fact, aberrations induced by lateral wave speed heterogeneities strongly degrade the transverse resolution of the readoutting process. Such phase distortions fully blur the confocal images and prevent us from any interpretation. The following section describes how these aberrations can be quantified from the FR matrix.

E. Quantification of aberrations

The FR matrix can provide more than a confocal image since its off-diagonal elements can lead to a quantification of aberrations. To that aim, a relevant observable is the distribution of the mean backscattered intensity as a function of the relative position $\Delta \boldsymbol{\rho}$ between the input and output focusing points [15, 20]:

$$I(\Delta \boldsymbol{\rho}, z) = \langle |R(\boldsymbol{\rho} - \Delta \boldsymbol{\rho}/2, \boldsymbol{\rho} + \Delta \boldsymbol{\rho}/2, z)|^2 \rangle_{\boldsymbol{\rho}}. \quad (12)$$

where the symbol $\langle \dots \rangle$ accounts for an average over the variable in the subscript. To express this quantity theoretically, we first make an isoplanatic approximation that consists in assuming input and output PSFs as spatially-invariant $H(\boldsymbol{\rho}, \boldsymbol{\rho}_{\text{in/out}}, z) = H(\boldsymbol{\rho} - \boldsymbol{\rho}_{\text{in/out}}, z)$. Under this assumption and in the speckle regime (*i.e* random subsurface reflectivity), the mean intensity profile is shown to be proportional to the convolution between the incoherent output and input local PSF, independently from the medium's reflectivity[15]:

$$\langle I(\Delta \boldsymbol{\rho}, z) \rangle \propto \left[|H|^2 \overset{\Delta \boldsymbol{\rho}}{\otimes} |H|^2 \right] (\Delta \boldsymbol{\rho}, z) \quad (13)$$

In the following, we will refer to this quantity as the reflection point spread function (RPSF). The RPSF is a direct indicator of the focusing quality and its spatial extension directly provides the

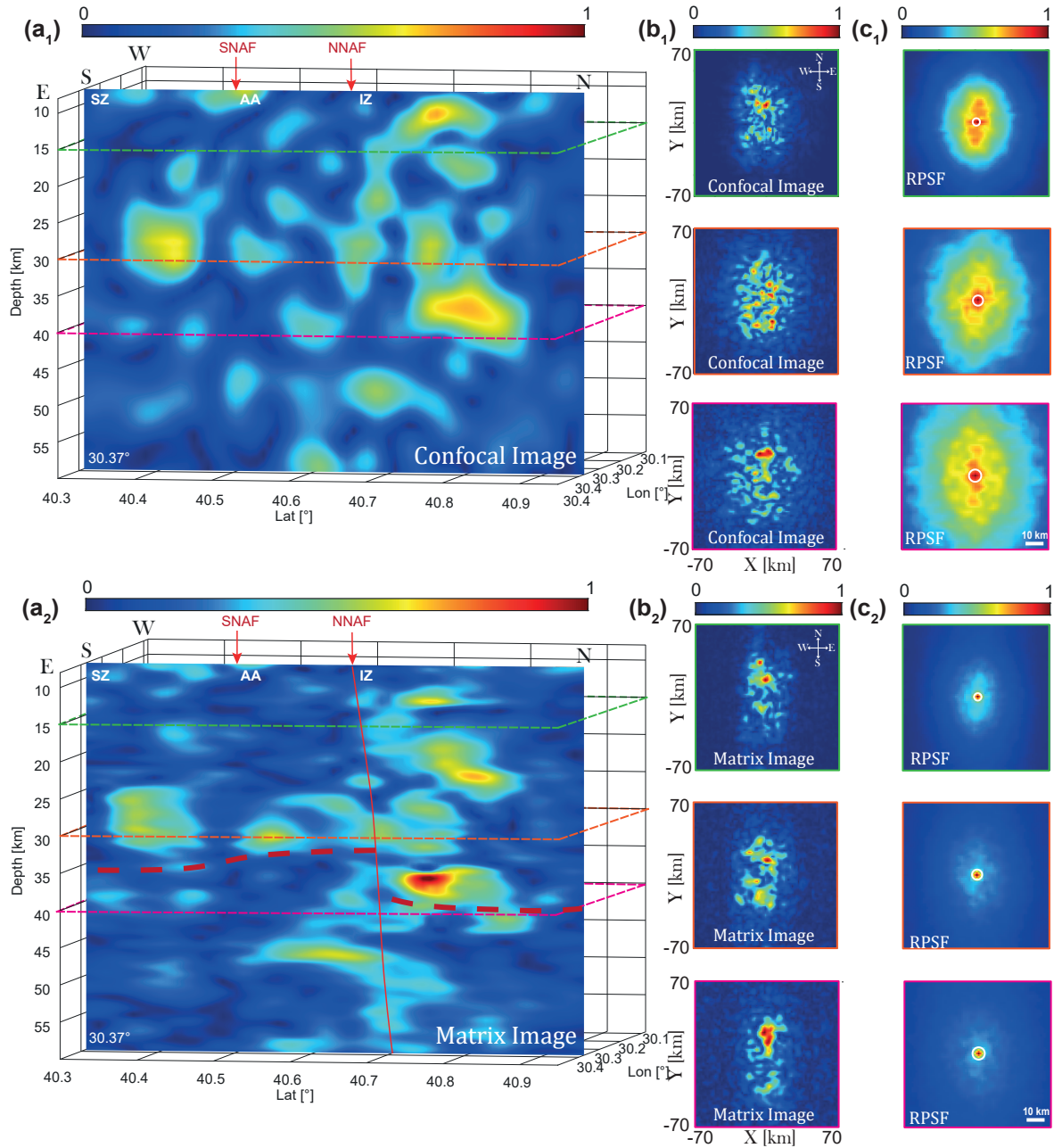


FIG. 3: Vertical North-South cross-sections at 30.37°E and depth slices from (1) the original and (2) the final 3D scattering volume. (a) The North-South profile is oriented perpendicular to the fault traces. The location of the profile is shown in Fig. 1a. The locations of the southern (SNAF) and northern (NNAF), and the major crustal blocks (SZ: Sakarya zone, AA: Armutlu-Almacik and IZ: Istanbul zone) are labeled. The interpreted location of the fault at depth are indicated by a red line. The color scale refers to the scattering intensity. It is normalized by the maximum value of the scattering energy inside the volume. Our interpretation of the Moho's location is indicated by red dashed lines. (b) Depth slices retrieved from the 3D scattering volume at $z = 15, 30$ and 40 km with (c) their corresponding RPSFs.

transverse resolution of the confocal image.

Fig. 2c displays the RPSF averaged over the whole field-of-view at depth $z = 25$ km. For sake of comparison, Fig. 2d shows the ideal (i.e diffraction-limited) RPSF that would be obtained in absence of aberrations. The comparison between Figs. 2c and d highlights the impact of aberrations and the mismatch between the wave velocity model of Table I and the real wave speed distribution. Indeed, the full width at half maximum w of the intensity profile is increased by a factor ~ 6 compared to its diffraction-limited value (white circle in Fig. 2d, Eq. 11) at depth $z = 25$ km. It explains the blurred aspect of the confocal image displayed in Fig. 2e at the same depth. The impact of aberrations is also depicted by Fig. 3c₁ that displays the depth evolution of the RPSF inside the Earth. As the diffraction-limited resolution (Eq. 11), the transverse extension of the RPSF also increases with z but it shows a much larger extension.

In the following we will show how matrix imaging can restore an optimal resolution for this image.

III. Exploiting the input-output angular correlations of the wave-field: The CLASS algorithm

In order to compensate for aberrations, the reflection matrix can be first projected in the plane wave basis:

$$\mathbf{R}_{\mathbf{k}\mathbf{k}}(z) = \mathbf{P}'_0(z) \times \mathbf{R}_{\boldsymbol{\rho}\boldsymbol{\rho}}(z) \times \mathbf{P}'_0{}^\top(z), \quad (14)$$

where the symbol \top stands for matrix transpose. Each coefficient of the matrix $\mathbf{R}_{\mathbf{k}\mathbf{k}}(z) = [R(\mathbf{k}_{\text{out}}, \mathbf{k}_{\text{in}}, z)]$ contains the reflected wave-field in the far field between input and output transverse wave vectors \mathbf{k}_{in} and \mathbf{k}_{out} . The matrix $\mathbf{R}_{\mathbf{k}\mathbf{k}}$ can be expressed as follows:

$$\mathbf{R}_{\mathbf{k}\mathbf{k}}(z) = \mathbf{T}(z) \times \boldsymbol{\Gamma}(z) \times \mathbf{T}^\top(z), \quad (15)$$

The matrix $\boldsymbol{\Gamma}$ describes the scattering process in the focused basis. This matrix is diagonal in the single scattering regime, and its coefficients then correspond to the true reflectivity $\gamma(\boldsymbol{\rho}, z)$ at depth z .

In the isoplanatic limit, the aberrations can be modelled by a far-field phase screen of transmittance $\tilde{\mathbf{H}} = [\tilde{H}(\mathbf{k}_{\parallel})]$, such that $\mathbf{T} = \tilde{\mathbf{H}} \circ \mathbf{P}'_0$, and where $\tilde{H}(\mathbf{k}_{\parallel}) = \int d\mathbf{r} H(\boldsymbol{\rho}) e^{-i\mathbf{k}_{\parallel} \cdot \boldsymbol{\rho}}$ is the Fourier transform of the input or output PSF $H(\boldsymbol{\rho})$. Under this approximation, a theoretical expression of $\mathbf{R}_{\mathbf{k}\mathbf{k}}$ can be derived in the single scattering regime [16]:

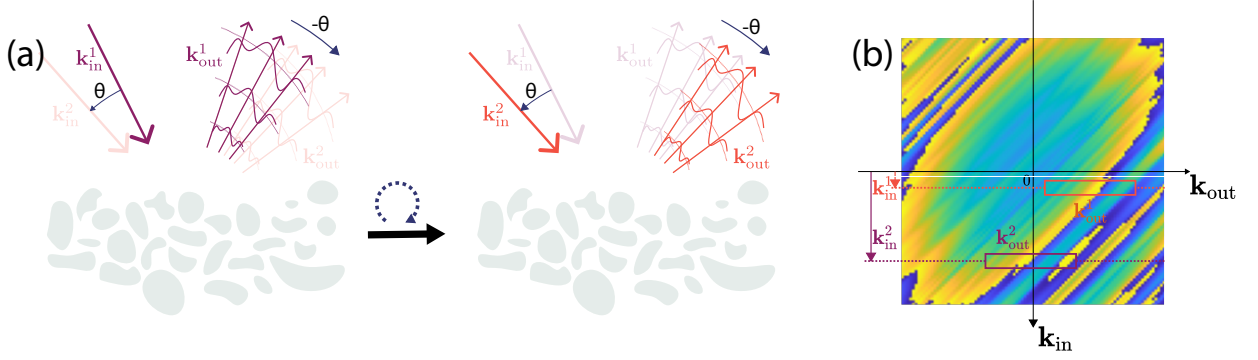


FIG. 4: Manifestation of the memory effect in the plane wave basis. (a) When an incident plane wave is rotated by an angle θ , the reflected wave-field is shifted by the opposite angle $-\theta$. (b)

This memory effect results in a deterministic coherence along the antidiagonals ($\mathbf{k}_{\text{in}} + \mathbf{k}_{\text{out}} = \text{constant}$) of the reflection matrix \mathbf{R}_{kk} expressed in the plane wave basis. The phase of a matrix \mathbf{R}_{kk} is displayed for sake of illustration. This matrix has been obtained from an ultrasound experiment performed on a medium of random reflectivity (acoustic phantom) in the conditions described by [15].

$$R(\mathbf{k}_{\text{out}}, \mathbf{k}_{\text{in}}, z) = \tilde{H}(\mathbf{k}_{\text{in}}) \tilde{\gamma}(k_{\text{in}} + k_{\text{out}}, z) \tilde{H}(\mathbf{k}_{\text{out}}), \quad (16)$$

where $\tilde{\gamma}(\mathbf{k}_{\parallel}, z) = \int d\boldsymbol{\rho} \gamma(\boldsymbol{\rho}, z) \exp(-i\mathbf{k}_{\parallel} \cdot \boldsymbol{\rho})$ is the 2D Fourier transform of the medium's reflectivity $\gamma(\boldsymbol{\rho}, z)$.

In the single scattering regime and in absence of aberrations ($\tilde{H}(\mathbf{k}_{\parallel}) \equiv 1$), the reflection matrix expressed in the plane wave basis exhibits a deterministic coherence along its antidiagonals ($\mathbf{k}_{\text{in}} + \mathbf{k}_{\text{out}} = \text{constant}$, see Fig. 4b) [51, 52]. This peculiar property is a manifestation of a phenomenon called the memory effect in wave physics [53, 54] (Fig. 4a). In the present case, this deterministic coherence is not checked because of the phase screen, $\tilde{H}(\mathbf{k}_{\parallel})$, in Eq. 16 that accounts for the phase distortions undergone by the incident and reflected wave-fronts (see Fig. 2a). The principle of the CLASS algorithm [17, 22, 23] consists in restoring this coherence by applying a phase correction, $\exp[-i\phi_C(\mathbf{k}_{\parallel})]$, at input and output of \mathbf{R}_{kk} :

$$R^{(C)}(\mathbf{k}_{\text{out}}, \mathbf{k}_{\text{in}}) = e^{-i\phi_C(\mathbf{k}_{\text{out}})} R(\mathbf{k}_{\text{out}}, \mathbf{k}_{\text{in}}) e^{-i\phi_C(\mathbf{k}_{\text{in}})}, \quad (17)$$

The corresponding wave-front, $\exp[i\phi_C(\mathbf{k}_{\parallel})]$, is actually an estimator of the aberration transmittance, $\tilde{H}(\mathbf{k}_{\parallel})$. The method to derive this estimator is described in Supplementary Section S2.

From the corrected matrix $\mathbf{R}_{\mathbf{k}\mathbf{k}}^{(C)}$, a CLASS FR matrix is obtained as follows:

$$\mathbf{R}_{\rho\rho}^{(C)}(z) = \mathbf{P}_0^\dagger(z) \times \mathbf{R}_{\mathbf{k}\mathbf{k}}^{(C)}(z) \times \mathbf{P}_0^{I*}(z) \quad (18)$$

A corrected confocal image is extracted from the diagonal of $\mathbf{R}_{\rho\rho}^{(C)}(z)$ and displayed in Fig. 5a at depth $z = 25$ km. It should be compared with the original image shown in Fig. 2e. While the latter one displays a random-like feature, the corrected image reveals a greater reflectivity in the North that can be correlated with the expected damage around the Northern branch of the fault. The comparison between these two images illustrates the benefit of the correction process. The gain in resolution can be assessed by looking at the backscattered intensity profile (Eq. 12) that allows to probe the RPSF averaged over the whole field-of-view (see Fig. 5c). Compared to the original RPSF displayed in Fig. 2c, we can notice that a large component of the off-diagonal energy has been brought back to the confocal lobe (white circle). The resolution w is reduced from 40 km to 8 km but it is still larger than the diffraction-limited resolution ($\delta\rho_0 \sim 6$ km at the considered depth). A diffuse component subsists and can be explained by the spatially-varying residual aberrations, $\delta\tilde{H}(\mathbf{k}_{||}, \mathbf{r})$, that have not been compensated by the CLASS algorithm, such that $\delta\tilde{H}(\mathbf{k}_{||}, \mathbf{r}) = \tilde{H}(\mathbf{k}_{||}, \mathbf{r})e^{-i\phi_C(\mathbf{k}_{||})}$.

A local compensation of higher order aberrations is thus required. This issue is handled in the following section by investigating the reflection matrix and its distorted component between the focused and plane wave bases.

IV. Matrix approach for adaptive focusing: The local distortion matrix

The distortion matrix \mathbf{D} was already introduced in ultrasound [16, 24], optics [18, 55] and seismology [20]. Several applications proved the efficiency of this matrix in overcoming aberrations and improve the image quality. Recent works in seismology [20] and optics [18] have shown that for certain scattering regimes (specular reflectors or sparse scattering), there was a one-to-one association between the eigenstates of \mathbf{D} and the isoplanatic patches present in the field-of-view. Here, this property does not hold because the NAFZ subsurface exhibits a continuous and random reflectivity (see Supplementary Section S1). In this speckle regime, local distortion matrices should be considered over restricted areas in which the isoplanatic hypothesis is ideally fulfilled [24, 55].

In this section, the distortion matrix concept is applied to the CLASS FR matrix obtained in

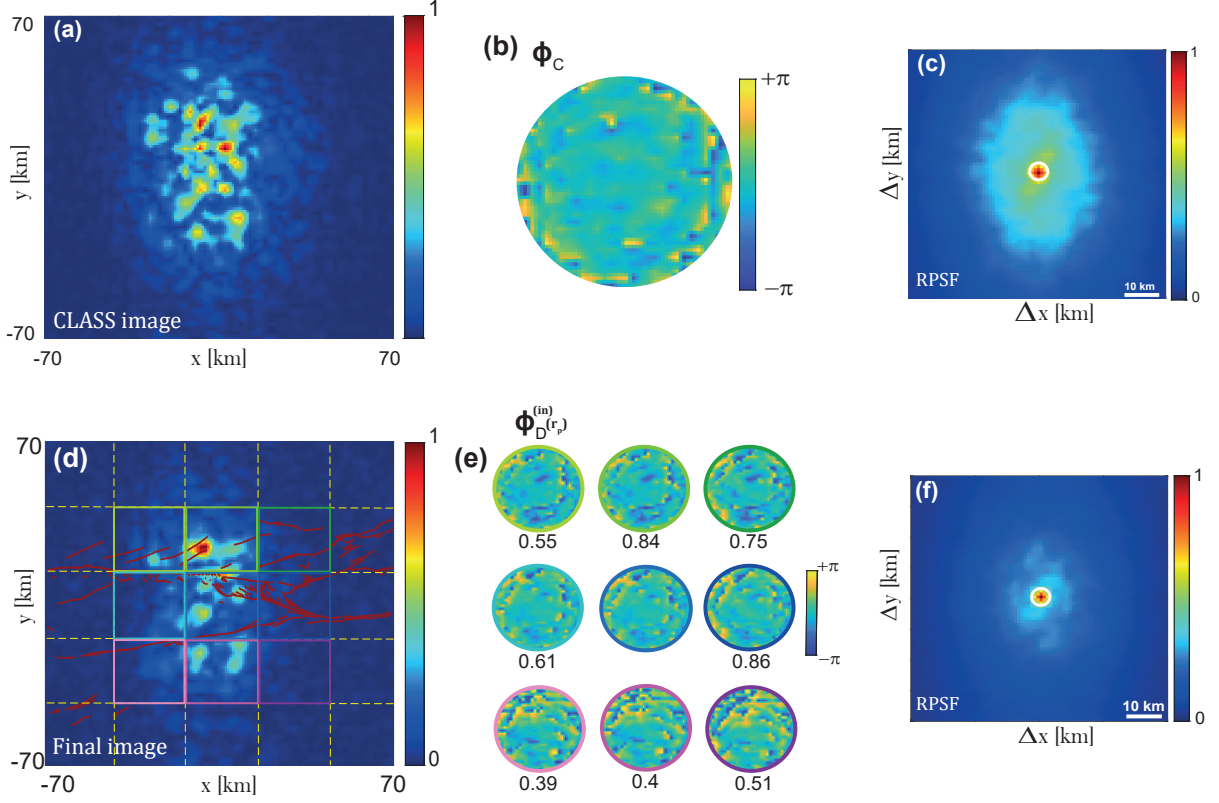


FIG. 5: Aberration correction process at $z = 25$ km. (a) Confocal image obtained after applying the conjugate of (b) the CLASS phase law ϕ_C computed at this depth. (b) RPSF obtained after CLASS correction. (c) RPSF obtained after performing four iteration steps of the distortion matrix process. (d) Confocal image obtained after performing four iteration steps of the distortion matrix process. The red lines represent the NAFZ fault traces at the surface. The yellow dashed lines delineate the regions over which a local aberration phase law $\phi(\mathbf{k}_{\parallel}, \mathbf{r})$ has been estimated. (e) Corresponding input aberration phase laws $\phi_{\mathbf{D}}^{(in)}(\mathbf{r}_p)$ obtained at the end of the process. The correlation coefficients between the corresponding aberration transmittances and the central one are displayed below each phase mask. (f) RPSF at the end of the matrix imaging process.

the previous section for compensation of spatially-distributed aberrations. The process is outlined by five steps: (i) projection of the CLASS FR matrix at output into the plane wave basis (Fig. 6a), (ii) the realignment of the reflected wave-fronts to form a distortion matrix $\mathbf{D} = [D(\mathbf{k}_{\text{out}}, \boldsymbol{\rho}_{\text{in}}, z)]$ (see Fig. 6b and Supplementary Section S3), (iii) the truncation of \mathbf{D} into local distortion matrices $\mathbf{D}'(\mathbf{r}_p)$, (iv) the singular value decomposition of $\mathbf{D}'(\mathbf{r}_p)$ to extract a residual aberration phase law for each point \mathbf{r}_p (see Fig. 6e and Supplementary Section S4) and build an estimator of the transmission matrix \mathbf{T} (Fig. 6f); (v) the phase conjugation of \mathbf{T} to correct for output residual aberrations (Fig. 6g). All of these steps are then repeated by exchanging output and input bases.

The first two steps have already been described by [20]. Therefore we will focus here on the

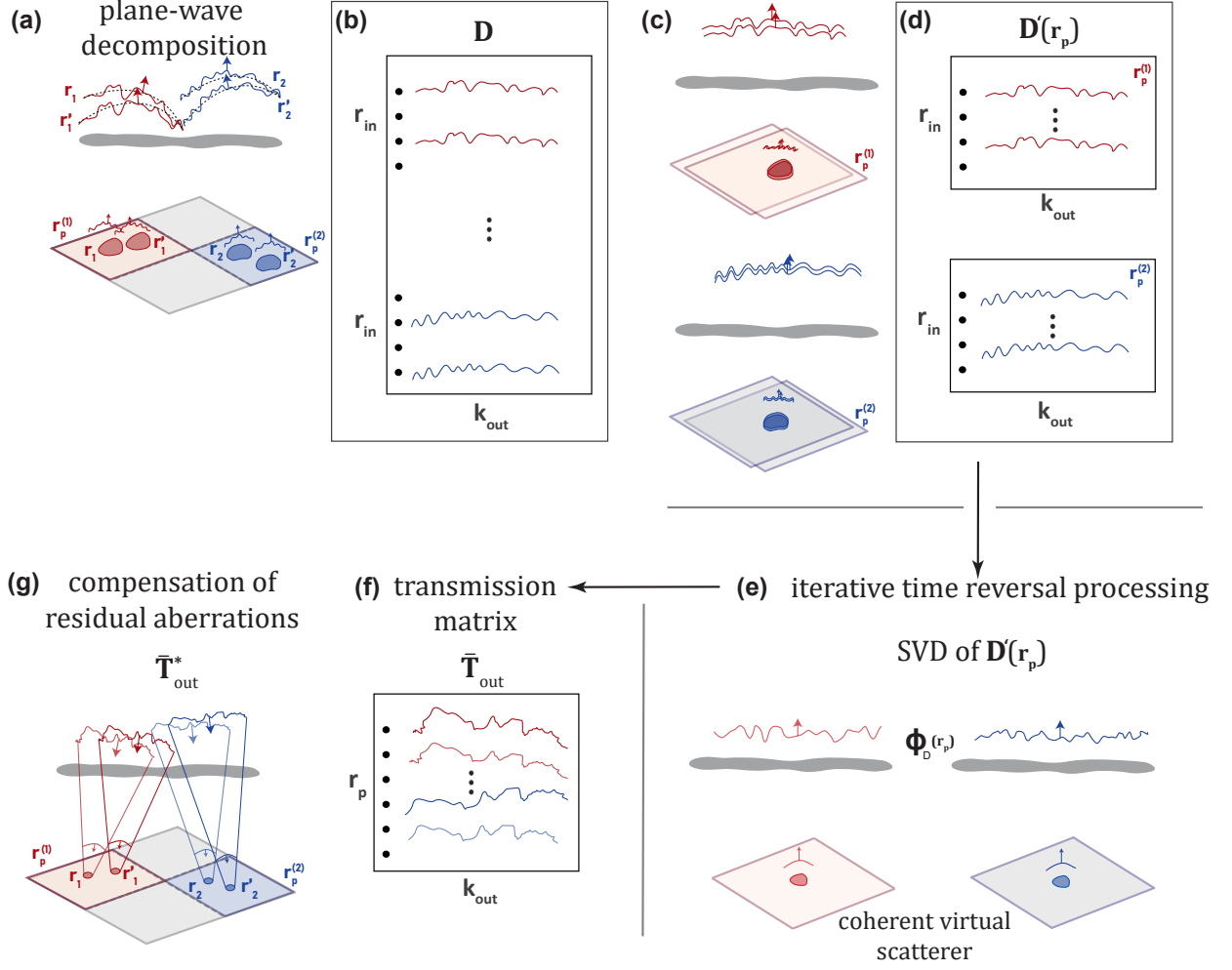


FIG. 6: Local aberration correction. (a) One-side plane wave decomposition of each CLASS matrix yields the reflected wave-front associated with each focusing point r_{in} . (b) By removing the geometrical curvature of each reflected wavefront, the resulting distortion matrix D only contains the aberrated component of those wavefronts. (c) This operation consists in realigning those wavefronts as if they were generated by input focal spots virtually shifted at the origin. (d) The distortion matrix D is truncated over a set of spatial windows identified by their mid-point r_p , a set of local distortion matrices $D'(r_p)$. (e) Their singular value decomposition yields an aberration phase law for each spatial window by combining coherently each focal spot to synthesize a virtual coherent reflector. (f) The aberration phase law obtained in each patch forms the estimator \bar{T} of the transmission matrix. (g) The phase conjugate of \bar{T} provides the focusing laws to compensate for the phase distortions for each patch r_p .

local aspect of the D -matrix analysis. Our strategy is to divide the field-of-view into a set of overlapping regions (Fig. 5d). Each region is defined by a central midpoint $r_p = (\rho_p, z_p)$ and a spatial extension L . For each region, the local residual D -matrix is defined as:

$$D'(k_{out}, \rho_{in}, r_p) = D(k_{out}, \rho_{in}, z_p)W(\rho_{in} - \rho_p), \quad (19)$$

where $W(\boldsymbol{\rho})$ is a spatial window function such that $W(\boldsymbol{\rho}) = 1$ for $|x| < L$ and $|y| < L$, and zero elsewhere. Ideally, wave-front distortions should be invariant over each region, meaning that the virtual sources $\mathbf{r}_{\text{in}} = (\boldsymbol{\rho}_{\text{in}}, z)$ associated with each region belong to the same isoplanatic patch. However, in practice, this hypothesis is not fully verified. The isoplanatic length actually scales as the typical transverse dimension over which the wave velocity fluctuates. On the one hand, the dimension L of the window function should therefore be reduced to cover the smallest isoplanatic region as possible in order to provide a local and sharp measurement of aberrations. On the other hand, it should also be large enough to include a sufficient number of realizations of disorder in order to unscramble the effect of aberrations from the medium's reflectivity [24]. To reach a good estimation of the aberration phase law, the number of input focusing points in each region should be one order of magnitude larger than the number of resolution cells mapping the CLASS focal spot (Fig. 5c) [16]. This is why the initial CLASS step was important to initiate the aberration correction process and reduce the extension of the focal spots before a local and finer compensation of residual aberration by means of the **D**-matrix concept. The area covered by the CLASS focal spot being of $20 \times 14 \text{ km}^2$ (Fig. 5c), the extent of the window is chosen to be $55 \times 55 \text{ km}^2$.

To extract a local estimation of the aberration transmittance $\delta\tilde{\mathbf{H}}(\mathbf{r}_p)$, a singular value decomposition of each sub-matrix $\mathbf{D}'(\mathbf{r}_p)$ is applied (see Fig. 6e and Supplementary Section S4). The phase of the first output singular vector, $\phi_D^{(\text{out})}(\mathbf{r}_p)$, directly provides an estimator of the transmission matrix, such that:

$$\bar{\mathbf{T}}_{\text{out}} = \mathbf{P}'_0 \circ e^{i[\phi_D^{(\text{out})}(\mathbf{r}_p) + \phi_C^{(\text{out})}(z_p)]} \quad (20)$$

The phase conjugate of $\bar{\mathbf{T}}_{\text{out}}$ provides the focusing laws to compensate for the output phase distortions over each patch (Fig. 6f). The same method can be repeated by exchanging the focused and Fourier bases between input and output in order to estimate the transmission matrix \mathbf{T}_{in} [20]. The whole process is iterated once to refine the estimation of \mathbf{T}_{out} and \mathbf{T}_{in} .

The input phase laws obtained at the end of the aberration correction process are displayed in Fig. 5e for the central regions of the field-of-view highlighted in Fig. 5d. Although they show some similar features (in particular the low spatial frequency components), they also display some differences that are quantified by the correlation coefficient between the different phase masks with the central one. The value of this coefficient is reported below each phase mask. This correlation

coefficient goes from 0.86 for closest spatial windows to 0.39 for the furthest ones. One can also notice that clear differences in the phase laws can be observed between the north, center and the south of the field-of-view. The presence of these lateral differences is consistent with the three geological blocks in the region (Fig. 1b). The latter observation together with the correlation coefficient value show the importance of estimating a different phase law for each area and justifies the implementation of a local aberration correction process.

Using $\bar{\mathbf{T}}_{\text{out}}$ and $\bar{\mathbf{T}}_{\text{in}}$, a corrected FR matrix can be finally obtained:

$$\mathbf{R}_{\text{rr}}^{(D)}(z) = \bar{\mathbf{T}}_{\text{out}}^\dagger \times \mathbf{R}_{\text{kk}}(z) \times \bar{\mathbf{T}}_{\text{in}}^* \quad (21)$$

The corresponding confocal image and RPSF are displayed at $z = 25$ km in Figs. 5(d) and (f). The comparison with their CLASS counterparts [Figs 5(a) and (c)] shows the interest of the local D–matrix analysis. The diffuse background is clearly reduced and the RPSF is nearly similar to its ideal value (Fig. 2d), with almost all the backscattered energy contained in the white circle accounting for the diffraction limit. The residual background in Fig. 5f is probably associated with high-order aberrations whose coherence length (isoplanatic area) is smaller than the size L of the window function $W(\boldsymbol{\rho})$.

Correction steps	0	1	2	3	4	5	6
Correction type	0	CLASS	CLASS	D	D	D	D
Correction side		Output	Input	Output	Input	Output	Input
Confocal gain (dB)		2.41	5.17	7.1	9	9.16	9.26
Resolution w (km)	40	20	8	7	6	6	6

TABLE II: Confocal gain and resolution at each step of the aberration correction process.

To be more quantitative, a confocal gain can be computed from the intensity ratio between the corrected (Fig. 5a and d) and initial (Fig. 2e) images. The transverse resolution can also be estimated from the full width at half maximum w of the RPSF. The confocal gain and the resolution are reported in Table II at each step of the aberration correction process for depth $z = 25$ km. Strikingly, the transverse resolution is enhanced by a factor ~ 7 compared with its initial value and the confocal intensity is increased by more than 9 dB. These values highlight the benefit of matrix imaging for in-depth probing of NAFZ at a large scale.

In the next section, the 3D image of the medium around the NAFZ is now revealed by combining the images derived at each depth. A structural interpretation is then provided in light of previous studies on the NAFZ.

V. 3D structure of the NAFZ

The previous sections have shown the process for a local compensation of phase distortions. Performing this correction process at each depth allows to uncover a well-resolved 3D image of the subsurface.

Figure 3a₂ shows a North-South cross-section from the final 3D image. This cross-section is chosen at the same location as the one in Fig. 3a₁ and crosses the two fault strands. It also spans the three geological units: Istanbul zone (IZ), Armutlu-Almacik (AA) and Sakarya zone (SZ). The scattering generated by the heterogeneities of the medium induce a decrease of the backscattered energy with depth. Consequently, a drop of amplitude is observed in the 3D images. In order to compensate for this, the intensity in the cross-sections is normalized by the mean intensity calculated at each depth.

Three depth slices retrieved from the final 3D images at $z = 15, 30$ and 40 km are also represented in Figs. 3b₂ with their corresponding RPSFs in Figs. 3c₂. Compared to the initial RPSFs (Figs. 3c₁), the resolution is significantly improved by a factor that goes from 7 at small depth ($z < 15$ km) to 9 beyond $z = 40$ km. The final matrix images in Figs. 3b₂ can also be compared to the initial confocal ones in Figs. 3b₁. While the original images show random-like features, the images obtained after aberration correction reveal better defined features and a reflectivity that is mainly concentrated in the North. The same observation can be made by looking at the corrected cross-section in Fig. 3a₂. The differences between the corrected and raw cross-sections are pronounced. While in the raw image, no clear structures and layers are visible, the corrected image reveals sub-horizontal structures with a refined level of details, thanks to the drastic gain in resolution revealed by the RPSF.

Due to its significant seismic activity over the past 100 years, and to assess the ongoing hazard posed by this activity, extensive research has been conducted on the NAFZ to image its structure and determine its mechanical characteristics. The scattering structure in Fig. 3a₂ is interpreted with reference to prior studies conducted in the region.

The first thing to notice in the profiles is that the scattered energy is predominantly situated in the North, which corresponds with the location of the Northern branch. This observation may be associated with the greater seismic activity of the Northern strand compared to the seismic activity of the Southern strand. The scattering below this strand and North of it, that extends to at least 60 km, can be explained by the damage caused by the large deformation of this complex fault system

with a cumulative slip of the order of 80 km [56, 57] during the last million years as well as the heterogeneities that have been inherited from the complex tectonic history of the region.

At the east of the Sea of Marmara, the Moho depth was reported to be between 30 and 35 km [58, 59]. A deepening of the Moho was identified (~ 40 km) in the IZ by [60], [61], [34], [35], [62] and [63]. In Fig. 3a₂, a high scattering zone is observed between 25 and 40 km depth corresponding to a heterogeneous lower crust. Its lower boundary indicates the presence of the Moho (red dashed line). The Moho depth varies from 35 km in the South to 42 km in the North. The reflectivity is disrupted around 40.75°N suggesting the presence of a step in the Moho below the Northern strand. The latter observation is in agreement with previous studies [62, 63]. Below the Moho, reflective structures are observed, mainly beneath AA and IZ, in agreement with [47]. These findings, supported with other studies [35, 47, 62, 63], suggest that the NNAF cuts through the entire crust and reaches the upper mantle [35, 47, 62, 63]. The signature of the NAFZ in the mantle has been proposed by the long period analysis of [36].

The signature of the Northern strand at depth can be identified by the presence of discontinuities in the scattering distribution in the first 20 km of the crust (Fig. 3a₂) and also by the termination of sub-Moho structures below the Northern strand. The Southern strand, on the other hand, lacks significant scattering, indicating that it has a weaker signal compared to the Northern strand. This, along with the continuity of the Moho in the South, suggests that the SNAF is confined in the crust and does not extend to the upper mantle, Armutlu block being a crustal structure.

In this section, only one cross-section has been depicted to demonstrate the significant enhancements and the gain in resolution provided by the presented matrix approach. A more in-depth analysis of the scattering volume around the NAFZ will be provided in a future study.

VI. Conclusion

Matrix imaging provides unprecedented view of the NAFZ. To that aim, we exploited seismic noise data from a dense deployment over the rupture region of the 1999 Izmit earthquake. Ambient noise cross-correlations enable the passive measurement of the reflection matrix associated with the dense array of geophones. The body wave component is then used to image the in-depth reflectivity of the NAFZ subsurface. Compared with our previous work that considered a sparse scattering medium [20], the NAFZ case is more general since it exhibits both specular reflectors such as Moho discontinuity and a random distribution of heterogeneities.

The strength of matrix imaging lies in the fact that it does not require an accurate velocity model. Here, a layered velocity model is employed but strong phase distortions subsist since lateral variations of the wave velocity are not taken into account. Nevertheless, such complex aberrations are compensated by two matrix methods previously developed in optical microscopy [17, 23] and ultrasound imaging [15, 24]. First, the CLASS algorithm exploits angular correlations and memory effect exhibited by the reflection matrix to compensate for spatially-invariant aberrations. Second, a local analysis of the distortion matrix enables a local compensation of spatially-distributed aberrations. Together, those two approaches provide a sharp estimation of the transmission matrix between the Earth surface and the subsurface, leading to a narrowing of the imaging PSF by a factor that goes from 7 to 9. Therefore, a diffraction-limited resolution is reached for any pixel of the image.

Thanks to matrix imaging, the scattering structure of the crust and upper mantle of the NAFZ continental strike slip fault is thus revealed. The 60 km depth profile, show terminations of crustal discontinuities mainly below the northern branch. The localized scattering around the NNAF is consistent with the fact that it is the most seismically active fault and that it ruptured during the last 7.6 Izmit earthquake. We identify a step in the Moho coinciding with the surface location of this branch in the East of DANA network. Moreover, the scattering extends to the upper mantle in the North. All these observations are consistent with previous studies and suggest that the NNAFZ is localized in the crust and extends to the upper mantle.

Although spectacular, several points remain perfectible in the obtained image. First, potential conversion between shear and longitudinal waves is not considered by matrix imaging. Second, only a broadband compensation of phase distortions is performed. Yet, scattering phenomena or multiple reflections would require to go beyond the application of simple time delays to the impulse response between geophones. Finally, a reflectivity image is only qualitative since it does not directly quantify the mechanical properties of the subsurface. Yet matrix imaging offers the possibility of mapping the velocity distribution inside the medium [15]. This will be the focus of a future study.

Acknowledgments

This project has received funding from the European Research Council (ERC) under the European Union Horizon 2020 research and innovation program (grant agreement No 742335, F-

IMAGE and grant agreement No. 819261, REMINISCENCE).

Open Research

The data used for this study were recorded by the temporary array DANA and can be found using the following link: <http://www.fdsn.org/doi/10.7914/SN/YH2012>. Codes used to post-process the seismic data within this paper are available from the corresponding author upon reasonable request.

Supplementary Information

This supplementary material includes details about: (i) the study of the far-field reflection matrix to determine the nature of the scattering process; (ii) the CLASS algorithm; (iii) the distortion matrix; (iv) its singular value decomposition.

S1. Nature of the scattering process

The aberration correction process depends on the scattering regime we are facing. To determine it, the plane wave basis is particularly adequate [16]. This section shows how the $\mathbf{R}_{\mathbf{k}\mathbf{k}}$ -matrix (Eq. 14 of the accompanying paper) can indicate the nature of the scattering processes taking place in NAFZ.

Indeed, assuming that the mismatch between the wave velocity model and reality only induces phase distortions between plane waves ($|\tilde{H}(\mathbf{k})|=1$), the norm-square of $\mathbf{R}_{\mathbf{k}\mathbf{k}}$ -coefficients, $R(\mathbf{k}_{\text{out}}, \mathbf{k}_{\text{in}}, z)$, is shown to be independent of aberrations [16]:

$$|R(\mathbf{k}_{\text{out}}, \mathbf{k}_{\text{in}}, z)|^2 = |\tilde{\gamma}(\mathbf{k}_{\text{out}} + \mathbf{k}_{\text{in}}, z)|^2. \quad (\text{S1})$$

Each anti-diagonal of $\mathbf{R}_{\mathbf{k}\mathbf{k}}$ ($\mathbf{k}_{\text{out}} + \mathbf{k}_{\text{in}} = \text{constant}$) encodes one spatial frequency of the medium's reflectivity. The spatial frequency spectrum of the medium's reflectivity can be estimated by averaging the intensity of the backscattered wave-field along each anti-diagonal of $\mathbf{R}_{\mathbf{k}\mathbf{k}}$. The result is displayed in Figs. S1b and d at two different depths: $z = 25$ km and $z = 35$ km. The norm square of the spatial frequency spectrum $\tilde{\gamma}(\mathbf{k}_{\parallel}, z)$ reveals the nature of the scattering process inside the medium. At $z = 25$ km, the frequency spectrum shows a flat spatial frequency spectrum (Fig. S1(b)) which is a manifestation of a random reflectivity (Fig. S1(a)). This regime is often referred to as a speckle wave-field in ultrasound imaging [16]. At depth $z = 35$ km, $\tilde{\gamma}(\mathbf{k}_{\parallel}, z)$ still shows a flat background due to randomly distributed heterogeneities but it also exhibits an over-intensity in the vicinity of $\mathbf{k}_{\parallel} = \mathbf{0}$ (Fig. S1(d)). This peak in the spatial frequency domain is characteristic of a specular reflector (Fig. S1(c)) at that depth that may be associated with an interface between lower crust layers. From these two examples, we can see that the subsurface of NAFZ consists of a mix between specular reflectors and randomly distributed heterogeneities.

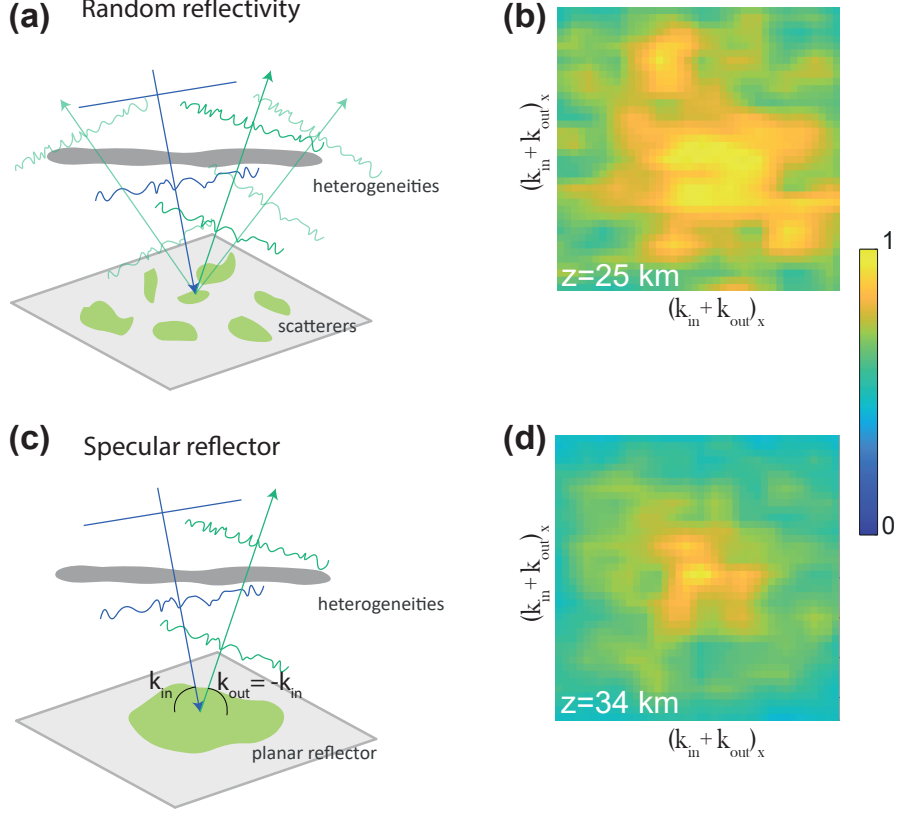


FIG. S1: Reflection matrix in the plane wave basis. (a) Sketch showing the angular decomposition of the reflected wave-field in the speckle regime for a plane wave illumination (blue). A set of plane waves (green) are reflected in all directions. (b) Spatial frequency spectrum of the reflectivity (Eq. S1) at $z = 25$ km. (c) Sketch showing the angular decomposition of the wave-field reflected by a planar interface. The incident plane wave (blue) is reflected with the same angle (green), such that $\mathbf{k}_{\text{out}} + \mathbf{k}_{\text{in}} = \mathbf{0}$; (d) Spatial frequency spectrum of the reflectivity (Eq. S1) at $z = 35$ km.

S2. CLASS algorithm

As stated in the accompanying paper, a full-field phase correction is first applied to the $\mathbf{R}_{\mathbf{k}\mathbf{k}}$ -matrix through the CLASS algorithm [17, 22]. The first step consists in a coherent sum of $\mathbf{R}_{\mathbf{k}\mathbf{k}}$ along its antidiagonals [see Fig. S2(a)]:

$$C(\mathbf{k}_+) = \sum_{\mathbf{k}_{\text{out}}} R(\mathbf{k}_{\text{out}}, \mathbf{k}_+ - \mathbf{k}_{\text{out}}) \quad (\text{S2})$$

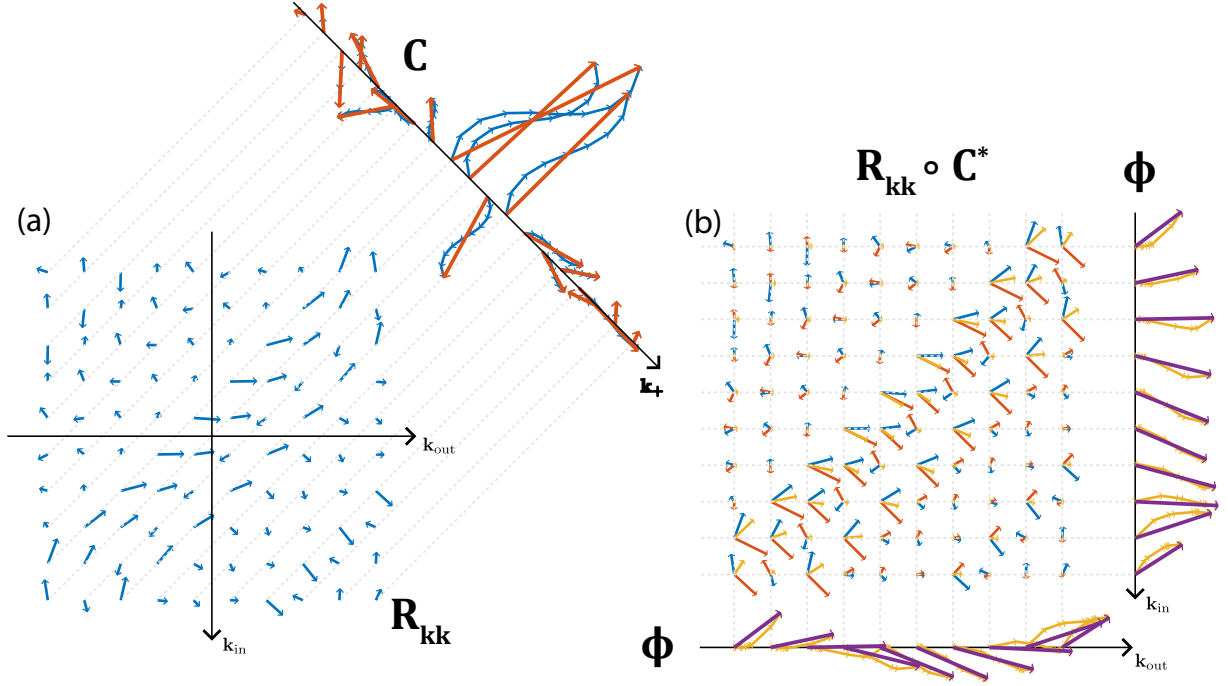


FIG. S2: Schematic of the CLASS algorithm. (a) First step (Eq. S2). The components of the $\mathbf{R}_{\mathbf{k}\mathbf{k}}$ -matrix are represented in the complex plane by blue arrows. Each antidiagonal of $\mathbf{R}_{\mathbf{k}\mathbf{k}}$ is summed coherently to provide the \mathbf{C} -vector, whose coefficients in the complex plane are displayed as red arrows. (b) Second and third steps (Eqs. S3 and S4). The Hadamard product between $\mathbf{R}_{\mathbf{k}\mathbf{k}}$ (red arrows) and \mathbf{C}^* (blue arrows) yields $\mathbf{R}'_{\mathbf{k}\mathbf{k}}$ (yellow arrows). The sum of its lines or columns yields the estimator ϕ (purple arrows).

with $\mathbf{k}_+ = \mathbf{k}_{\text{in}} + \mathbf{k}_{\text{out}}$. The second step consists in performing the Hadamard product between the phase conjugate of the resulting vector \mathbf{C} and the matrix $\mathbf{R}_{\mathbf{k}\mathbf{k}}$ [see Fig. S2(b)]:

$$R'(\mathbf{k}_{\text{out}}, \mathbf{k}_{\text{in}}) = R(\mathbf{k}_{\text{out}}, \mathbf{k}_{\text{in}}) C^*(\mathbf{k}_{\text{out}} + \mathbf{k}_{\text{in}}). \quad (\text{S3})$$

The last operation consists in compensating the phase of the reflectivity frequency spectrum $\gamma(\mathbf{k}_{\parallel}, z)$. An estimator of the phase distortion can be deduced by summing the columns of the compensated matrix $\mathbf{R}'_{\mathbf{k}\mathbf{k}}$ [see Fig. S2(b)]:

$$\phi_C(\mathbf{k}_{\text{out}}) = \arg \left[\sum_{\mathbf{k}_{\text{in}}} R'(\mathbf{k}_{\text{out}}, \mathbf{k}_{\text{in}}) \right], \quad (\text{S4})$$

In order to prove that $\phi_C(\mathbf{k}_{\parallel})$ is actually an estimator of $\arg \left\{ \tilde{H}(\mathbf{k}_{\parallel}) \right\}$ and to determine its bias, $\mathbf{R}_{\mathbf{k}\mathbf{k}}$ can be replaced by its expression (Eq. 15 of the accompanying paper) in Eqs. S2, S3 and S4.

It yields the following expression for ϕ_C :

$$\begin{aligned} \phi_C(\mathbf{k}_{\text{out}}) = & \arg \left[\tilde{H}(\mathbf{k}_{\text{out}}) \right] \\ & + \arg \left[\sum_{\mathbf{k}_{\text{in}}} |\tilde{\gamma}(\mathbf{k}_{\text{out}} + \mathbf{k}_{\text{in}}, z)|^2 \tilde{H}(\mathbf{k}_{\text{in}}) \sum_{\mathbf{k}'} \tilde{H}(\mathbf{k}') \tilde{H}^*(\mathbf{k}_{\text{out}} + \mathbf{k}_{\text{in}} - \mathbf{k}') \right]. \end{aligned} \quad (\text{S5})$$

The last expression shows that the estimator ϕ_C can be decomposed as a sum of its expectation $\arg \left[\tilde{H}(\mathbf{k}_{\text{out}}) \right]$ and its bias. For a medium of random reflectivity, the term $|\tilde{\gamma}(\mathbf{k}_{\text{out}} + \mathbf{k}_{\text{in}}, z)|^2$ can be replaced by its ensemble average, *i.e.* a constant. It yields:

$$\begin{aligned} \phi_C(\mathbf{k}_{\text{out}}) = & \arg \left[\tilde{H}(\mathbf{k}_{\text{out}}) \right] \\ & + \arg \left[H(0) \sum_{\mathbf{k}'} \tilde{H}(\mathbf{k}') \tilde{H}^*(\mathbf{k}_{\text{out}} + \mathbf{k}_{\text{in}} - \mathbf{k}') \right]. \end{aligned} \quad (\text{S6})$$

The last expression shows that the bias directly depends on the autocorrelation of the aberration phase law. The more complex the aberration is, the more biased its estimator is. It is equivalent to the bias exhibited by standard adaptive focusing methods induced by the blurring of a virtual guide star induced by focusing [24, 64].

S3. The distortion matrix

The output of the CLASS algorithm is a focused reflection matrix $\mathbf{R}_{\rho\rho}^{(C)}$ that still exhibits laterally-varying aberrations. To assess these residual aberrations, the first step is to chose a basis in which the distortion of the CLASS wave-front is the most spatially-invariant. In a horizontally multi-layered medium such as NAFZ, the plane-wave basis is the most adequate since plane waves are the propagation invariants in this geometry. A plane-wave projection consists in a spatial Fourier transform of the CLASS FR matrix $\mathbf{R}_{\mathbf{k}\rho}^{(C)}$:

$$\mathbf{R}_{\mathbf{k}\rho}^{(C)}(z) = \mathbf{P}'_0 \times \mathbf{R}_{\rho\rho}^{(C)}(z), \quad (\text{S7})$$

where \mathbf{P}'_0 is the Fourier transform operator defined by Eq. 5 of the accompanying paper. $\mathbf{R}_{\mathbf{k}\rho}^{(C)}(z) = [R^{(C)}(\mathbf{k}_{\text{out}}, \boldsymbol{\rho}_{\text{in}}, z)]$ connects each input focusing point $\mathbf{r}_{\text{in}} = (\boldsymbol{\rho}_{\text{in}}, z)$ to the CLASS wave-field in the plane wave basis (Fig. 6a of the accompanying paper).

The CLASS wave-field can be understood as a sum of two components: (i) a geometric component described by the reference matrix \mathbf{P}'_0 , containing the ideal wave-front generated by a source at \mathbf{r}_{in} according to the propagation model described in Table 1 of the accompanying paper (dashed black curves in Fig. 6a of the accompanying paper); (ii) a distorted component due to spatially distributed aberrations that subsists after the CLASS procedure described in Section 3 of the accompanying paper. The latter component refers to the residual phase distortions that should be isolated from the CLASS wave-field in order to be properly compensated. This can be done by subtracting the ideal wave-front that would be obtained in absence of aberrations (i.e the geometric component) from each CLASS wave-front induced by each input focusing wave at \mathbf{r}_{in} . Such operation can be expressed mathematically via a Hadamard product between $\mathbf{R}_{\mathbf{k}\rho}^{(C)}(z)$ and \mathbf{P}'_0 . It yields the residual distortion matrix $\mathbf{D}(z)$:

$$\mathbf{D}(z) = \mathbf{R}_{\mathbf{k}\rho}^{(C)}(z) \circ \mathbf{P}'_0^*, \quad (\text{S8})$$

The matrix $\mathbf{D}(z)$ connects any input virtual source \mathbf{r}_{in} to the residual distortion exhibited by the CLASS wave-field expressed in the plane wave basis (Figs. 6a and b of the accompanying paper). By removing the geometrical component of the CLASS wave-field, spatial correlations are highlighted between distorted wave-fields induced by neighbour virtual sources \mathbf{r}_{in} [18]. Such correlations are a manifestation of a spatial invariance of residual aberrations over areas generally referred to as isoplanatic patches [24].

Here, we investigate the case of speckle imaging (see Supplementary Section S1), in which fluctuations of the seismic wave velocity occur both in the lateral and axial directions. In this regime [24], the distortion matrix shall be investigated locally (Eq. 19 of the accompanying paper).

Text S4

Singular value decomposition of each local distortion matrix

Assuming the isoplanatic condition in each spatial window W_L , the coefficients of each distortion matrix $\mathbf{D}'(\mathbf{r}_p)$ matrix can be expressed as follows [24]:

$$D'(\mathbf{k}_{\text{out}}, \mathbf{r}_{\text{in}}, \mathbf{r}_p) = \delta\tilde{H}(\mathbf{k}_{\text{out}}, \mathbf{r}_p) \int d\mathbf{r} \gamma(\mathbf{r} + \mathbf{r}_{\text{in}}, z) \delta H(\mathbf{r}, \mathbf{r}_p) e^{i\mathbf{k}_{\text{out}} \cdot \mathbf{r}}, \quad (\text{S9})$$

Eq. S9 can be seen as a product between two terms: the output residual aberration transmittance and a virtual source term modulated by the medium's reflectivity $\gamma(\mathbf{r})$. In the following, we

will show how these two terms can be discriminated in order to get a proper estimation of the aberration transmittance $\delta\tilde{H}(\mathbf{k}_{\text{out}}, \mathbf{r}_p)$ at each point \mathbf{r}_p . This quantity is crucial since it will provide an estimator of the transmission matrix, $\mathbf{T} = \mathbf{P}'_0 \circ \tilde{\mathbf{H}}$, whose phase conjugate will directly provide the focusing laws to be applied for an optimized focus on each patch. To retrieve $\delta\tilde{H}(\mathbf{k}_{\text{out}}, \mathbf{r}_p)$, we will take advantage of the correlations that exist between each distorted wave-field in each patch (Fig. 6c and d of the accompanying paper). In practice, this can be done through an iterative time reversal analysis of each sub-matrix $\mathbf{D}'(\mathbf{r}_p)$.

Mathematically, it consists in a singular value decomposition (SVD) of each local distortion matrix $\mathbf{D}'(\mathbf{r}_p)$:

$$\mathbf{D}'(\mathbf{r}_p) = \mathbf{U}(\mathbf{r}_p) \times \mathbf{\Sigma}(\mathbf{r}_p) \times \mathbf{V}(\mathbf{r}_p)^\dagger \quad (\text{S10})$$

where $\mathbf{\Sigma}$ is a diagonal matrix containing the real positive singular values σ_i in a decreasing order $\sigma_1 > \sigma_2 > \dots > \sigma_N$. $\mathbf{U}(\mathbf{r}_p)$ and $\mathbf{V}(\mathbf{r}_p)$ are unitary matrices whose columns, $\mathbf{U}_i(\mathbf{r}_p) = [U_i(\mathbf{k}_{\text{out}}, \mathbf{r}_p)]$ and $\mathbf{V}_i(\mathbf{r}_p) = [V_i(\mathbf{r}_{\text{in}}, \mathbf{r}_p)]$, correspond to the output and input singular vectors, respectively. Under the isoplanicity condition, $\mathbf{D}'(\mathbf{r}_p)$ is, in first approximation, of rank 1 and the phase of the first singular vector, $\phi_D(\mathbf{r}_p) = [\text{arg}(U_{\text{out}}^{(1)}(\mathbf{k}_{\text{out}}, \mathbf{r}_p))]$ (Fig. 6e of the accompanying paper), yields an estimation of the aberration transmittance $\delta\tilde{\mathbf{H}}(\mathbf{r}_p)$ [24].

-
- [1] A. Sengör, The north anatolian transform fault: its age, offset and tectonic significance, *Journal of the Geological Society* **136**, 269 (1979).
- [2] A. Barka, The north anatolian fault zone, in *Annales tectonicae*, Vol. 6 (1992) pp. 164–195.
- [3] N. N. Ambraseys and C. Finkel, *The seismicity of Turkey and adjacent areas: a historical review, 1500-1800* (MS Eren, 1995).
- [4] R. S. Stein, A. A. Barka, and J. H. Dieterich, Progressive failure on the north anatolian fault since 1939 by earthquake stress triggering, *Geophysical Journal International* **128**, 594 (1997).
- [5] A. Vauchez, A. Tommasi, and D. Mainprice, Faults (shear zones) in the earth's mantle, *Tectonophysics* **558**, 1 (2012).
- [6] M. Campillo and P. Roux, Seismic imaging and monitoring with ambient noise correlations, *Treatise on Geophysics* **1**, 256 (2014).
- [7] M. Campillo and A. Paul, Long-range correlations in the diffuse seismic coda, *Science* **299**, 547 (2003).
- [8] N. M. Shapiro and M. Campillo, Emergence of broadband rayleigh waves from correlations of the ambient seismic noise, *Geophys. Res. Lett.* **31** (2004).
- [9] D. Draganov, K. Wapenaar, W. Mulder, J. Singer, and A. Verdel, Retrieval of reflections from seismic background-noise measurements, *Geophys. Res. Lett.* **34** (2007).
- [10] P. Poli, H. Pedersen, and M. Campillo, Emergence of body waves from cross-correlation of short period seismic noise, *Geophys. J. Int.* **188**, 549 (2012a).
- [11] P. Poli, M. Campillo, H. Pedersen, L. W. Group, *et al.*, Body-wave imaging of earth's mantle discontinuities from ambient seismic noise, *Science* **338**, 1063 (2012b).
- [12] L. Retailleau, P. Boué, L. Li, and M. Campillo, Ambient seismic noise imaging of the lowermost mantle beneath the North Atlantic Ocean, *Geophys. J. Int.* **222**, 1339 (2020).
- [13] D. Zigone, Y. Ben-Zion, M. Lehujeur, M. Campillo, G. Hillers, and F. L. Vernon, Imaging subsurface structures in the san jacinto fault zone with high-frequency noise recorded by dense linear arrays, *Geophysical Journal International* **217**, 879 (2019).
- [14] R. Qian and L. Liu, Imaging the active faults with ambient noise passive seismics and its application to characterize the huangzhuang-gaoliying fault in beijing area, northern china, *Engineering Geology* **268**, 105520 (2020).

- [15] W. Lambert, L. A. Cobus, M. Couade, M. Fink, and A. Aubry, Reflection matrix approach for quantitative imaging of scattering media, *Physical Review X* **10**, 021048 (2020a).
- [16] W. Lambert, L. A. Cobus, T. Frappart, M. Fink, and A. Aubry, Distortion matrix approach for ultrasound imaging of random scattering media, *Proc. Nat. Sci. Acad.* **117**, 14645 (2020b).
- [17] S. Kang, P. Kang, S. Jeong, Y. Kwon, T. D. Yang, J. H. Hong, M. Kim, K.-D. Song, J. H. Park, J. H. Lee, *et al.*, High-resolution adaptive optical imaging within thick scattering media using closed-loop accumulation of single scattering, *Nature communications* **8**, 1 (2017).
- [18] A. Badon, V. Barolle, K. Irsch, A. C. Boccara, M. Fink, and A. Aubry, Distortion matrix concept for deep imaging in optical coherence microscopy, *Sci. Adv.* **6**, eaay7170 (2020).
- [19] T. Blondel, J. Chaput, A. Derode, M. Campillo, and A. Aubry, Matrix approach of seismic imaging: application to the Erebus volcano, Antarctica, *J. Geophys. Res.: Solid Earth* **123**, 10,936 (2018).
- [20] R. Touma, T. Blondel, A. Derode, M. Campillo, and A. Aubry, A distortion matrix framework for high-resolution passive seismic 3-d imaging: application to the san jacinto fault zone, california, *Geophysical Journal International* **226**, 780 (2021).
- [21] E. Giraudat, A. Burtin, and A. Aubry, Passive seismic matrix imaging of la soufrière of guadeloupe volcano, in *EGU General Assembly Conference Abstracts* (2021) pp. EGU21–4516.
- [22] C. Choi, K.-D. Song, S. Kang, J.-S. Park, and W. Choi, Optical imaging featuring both long working distance and high spatial resolution by correcting the aberration of a large aperture lens, *Scientific reports* **8**, 1 (2018).
- [23] S. Yoon, H. Lee, J. H. Hong, Y.-S. Lim, and W. Choi, Laser scanning reflection-matrix microscopy for aberration-free imaging through intact mouse skull, *Nat. Commun.* **11**, 5721 (2020).
- [24] W. Lambert, L. A. Cobus, J. Robin, M. Fink, and A. Aubry, Ultrasound matrix imaging – part II: The distortion matrix for aberration correction over multiple isoplanatic patches, *IEEE Trans. Med. Imag.* **41**, 3921 (2022).
- [25] A. Barka, H. Akyuz, E. Altunel, G. Sunal, Z. Cakir, A. Dikbas, B. Yerli, R. Armijo, B. Meyer, J. De Chabalier, *et al.*, The surface rupture and slip distribution of the 17 august 1999 izmit earthquake (m 7.4), north anatolian fault, *Bulletin of the Seismological Society of America* **92**, 43 (2002).
- [26] H. Akyuz, R. Hartleb, A. Barka, E. Altunel, G. Sunal, B. Meyer, and v. R. Armijo, Surface rupture and slip distribution of the 12 november 1999 duzce earthquake (m 7.1), north anatolian fault, bolu, turkey, *Bulletin of the Seismological Society of America* **92**, 61 (2002).
- [27] R. Reilinger, S. McClusky, P. Vernant, S. Lawrence, S. Ergintav, R. Cakmak, H. Ozener, F. Kadirov,

- I. Guliev, R. Stepanyan, et al., Gps constraints on continental deformation in the africa-arabia-eurasia continental collision zone and implications for the dynamics of plate interactions, *Journal of Geophysical Research: Solid Earth* **111** (2006).
- [28] N. Ambraseys, Seismic sea-waves in the marmara sea region during the last 20 centuries, *Journal of Seismology* **6**, 571 (2002).
- [29] Y. Yılmaz, Ş. Genç, E. Yi?itbaş, M. Bozcu, and K. Yılmaz, Geological evolution of the late mesozoic continental margin of northwestern anatolia, *Tectonophysics* **243**, 155 (1995).
- [30] A. I. Okay and O. Tüysüz, Tethyan sutures of northern turkey, Geological Society, London, Special Publications **156**, 475 (1999).
- [31] F. Chen, W. Siebel, M. Satir, M. Terzioğlu, and K. Saka, Geochronology of the karadere basement (nw turkey) and implications for the geological evolution of the istanbul zone, *International Journal of Earth Sciences* **91**, 469 (2002).
- [32] M. K. Salah, S. Sahin, and M. Kaplan, Seismic velocity structure along the western segment of the north anatolian fault zone imaged by seismic tomography, *Bull. Earthq. Res. Inst. Univ. Tokyo* **82**, 209 (2007).
- [33] I. Koulakov, D. Bindi, S. Parolai, H. Grosser, and C. Milkereit, Distribution of seismic velocities and attenuation in the crust beneath the north anatolian fault (turkey) from local earthquake tomography, *Bulletin of the Seismological Society of America* **100**, 207 (2010).
- [34] E. Papaleo, D. G. Cornwell, and N. Rawlinson, Seismic tomography of the north anatolian fault: New insights into structural heterogeneity along a continental strike-slip fault, *Geophysical Research Letters* **44**, 2186 (2017).
- [35] E. Papaleo, D. Cornwell, and N. Rawlinson, Constraints on north anatolian fault zone width in the crust and upper mantle from s wave teleseismic tomography, *Journal of Geophysical Research: Solid Earth* **123**, 2908 (2018).
- [36] A. Fichtner, E. Saygin, T. Taymaz, P. Cupillard, Y. Capdeville, and J. Trampert, The deep structure of the north anatolian fault zone, *Earth and Planetary Science Letters* **373**, 109 (2013).
- [37] Y. Çubuk-Sabuncu, T. Taymaz, and A. Fichtner, 3-d crustal velocity structure of western turkey: Constraints from full-waveform tomography, *Physics of the Earth and Planetary Interiors* **270**, 90 (2017).
- [38] G. Taylor, S. Rost, G. A. Houseman, and G. Hillers, Near-surface structure of the north anatolian fault zone from rayleigh and love wave tomography using ambient seismic noise, *Solid Earth* **10**, 363 (2019).

- [39] G. Bensen, M. Ritzwoller, M. Barmin, A. L. Levshin, F. Lin, M. Moschetti, N. Shapiro, and Y. Yang, Processing seismic ambient noise data to obtain reliable broad-band surface wave dispersion measurements, *Geophysical Journal International* **169**, 1239 (2007).
- [40] M. S. Longuet-Higgins, A theory of the origin of microseisms, *Philosophical Transactions of the Royal Society of London. Series A, Mathematical and Physical Sciences* **243**, 1 (1950).
- [41] K. Hasselmann, A statistical analysis of the generation of microseisms, *Reviews of Geophysics* **1**, 177 (1963).
- [42] L. Stehly, M. Campillo, and N. Shapiro, A study of the seismic noise from its long-range correlation properties, *Journal of Geophysical Research: Solid Earth* **111** (2006).
- [43] Ö. Emre, T. Y. Duman, S. Özalp, F. Şaroğlu, Ş. Olgun, H. Elmacı, and T. Çan, Active fault database of turkey, *Bulletin of Earthquake Engineering* **16**, 3229 (2018).
- [44] K. Akbayram, C. C. Sorlien, and A. I. Okay, Evidence for a minimum 52 ± 1 km of total offset along the northern branch of the north anatolian fault in northwest turkey, *Tectonophysics* **668**, 35 (2016).
- [45] A. Berkhout, Wave field extrapolation techniques in seismic migration, a tutorial, *Geophysics* **46**, 1638 (1981).
- [46] A. J. Berkhout and C. P. A. Wapenaar, A unified approach to acoustical reflection imaging. II: The inverse problem, *J Acoust. Soc. Am.* **93**, 2017 (1993).
- [47] M. Kahraman, D. G. Cornwell, D. A. Thompson, S. Rost, G. A. Houseman, N. Türkelli, U. Teoman, S. A. Poyraz, M. Utkucu, and L. Gülen, Crustal-scale shear zones and heterogeneous structure beneath the north anatolian fault zone, turkey, revealed by a high-density seismometer array, *Earth and Planetary Science Letters* **430**, 129 (2015).
- [48] A. E. Karahan, H. Berckhemer, and B. Baier, Crustal structure at the western end of the north anatolian fault zone from deep seismic sounding, *Ann. Geophys.*, **44** (2001).
- [49] W. Lambert, J. Robin, L. A. Cobus, M. Fink, and A. Aubry, Ultrasound matrix imaging – part I: The focused reflection matrix, the F-factor and the role of multiple scattering, *IEEE Trans. Med. Imag.* (2022).
- [50] M. Born and E. Wolf, Principles of optics (Seventh edition) (Cambridge University Press, Cambridge, 2003).
- [51] A. Aubry and A. Derode, Detection and imaging in a random medium : A matrix method to overcome multiple scattering and aberration, *J. Appl. Phys.* **106**, 044903 (2009).
- [52] S. Kang, S. Jeong, H. Choi, W. Ko, T. D. Yang, J. H. Joo, J.-S. Lee, Y.-S. Lim, Q.-H. Park, and

- W. Choi, Imaging deep within a scattering medium using collective accumulation of single-scattered waves, *Nat. Photonics* **9**, 1 (2015).
- [53] I. Freund, M. Rosenbluh, and S. Feng, Memory effects in propagation of optical waves through disordered media, *Physical review letters* **61**, 2328 (1988).
- [54] S. Shahjahan, A. Aubry, F. Rupin, B. Chassignole, and A. Derode, A random matrix approach to detect defects in a strongly scattering polycrystal: How the memory effect can help overcome multiple scattering, *Appl. Phys. Lett.* **104**, 234105 (2014).
- [55] U. Najar, V. Barolle, P. Balondrade, M. Fink, A. C. Boccara, M. Fink, and A. Aubry, Non-invasive retrieval of the transmission matrix for optical imaging deep inside a multiple scattering medium, *hal: 03981863* (2023).
- [56] R. Armijo, B. Meyer, A. Hubert, and A. Barka, Westward propagation of the north anatolian fault into the northern aegean: Timing and kinematics, *Geology* **27**, 267 (1999).
- [57] M. Bohnhoff, P. Martínez-Garzón, F. Bulut, E. Stierle, and Y. Ben-Zion, Maximum earthquake magnitudes along different sections of the north anatolian fault zone, *Tectonophysics* **674**, 147 (2016).
- [58] E. Zor, E. Sandvol, C. Gürbüz, N. Türkelli, D. Seber, and M. Barazangi, The crustal structure of the east anatolian plateau (turkey) from receiver functions, *Geophysical Research Letters* **30** (2003).
- [59] E. Vanacore, T. Taymaz, and E. Saygin, Moho structure of the anatolian plate from receiver function analysis, *Geophysical Journal International* **193**, 329 (2013).
- [60] A. Frederiksen, D. Thompson, S. Rost, D. Cornwell, L. Gülen, G. Houseman, M. Kahraman, S. Poyraz, U. Teoman, N. Türkelli, *et al.*, Crustal thickness variations and isostatic disequilibrium across the north anatolian fault, western turkey, *Geophysical Research Letters* **42**, 751 (2015).
- [61] G. Taylor, S. Rost, and G. Houseman, Crustal imaging across the north anatolian fault zone from the autocorrelation of ambient seismic noise, *Geophysical Research Letters* **43**, 2502 (2016).
- [62] S. Rost, G. Houseman, A. Frederiksen, D. Cornwell, M. Kahraman, S. Altuncu Poyraz, U. Teoman, D. Thompson, N. Türkelli, L. Gülen, *et al.*, Structure of the northwestern north anatolian fault zone imaged via teleseismic scattering tomography, *Geophysical Journal International* **227**, 922 (2021).
- [63] J. Jenkins, S. N. Stephenson, P. Martínez-Garzón, M. Bohnhoff, and M. Nurlu, Crustal thickness variation across the sea of marmara region, nw turkey: A reflection of modern and ancient tectonic processes, *Tectonics* **39**, e2019TC005986 (2020).
- [64] S. Flax and M. O'Donnell, Phase-aberration correction using signals from point reflectors and diffuse scatterers: Basic principles, *IEEE transactions on ultrasonics, ferroelectrics, and frequency control* **35**,

758 (1988).